

Generation of circularly polarized high harmonic radiation using a transmission multilayer quarter waveplate

Jürgen Schmidt,^{1,*} Alexander Guggenmos,^{1,2} Michael Hofstetter,¹ Soo Hoon Chew,^{1,2} and Ulf Kleineberg¹

¹Faculty of Physics, Ludwig-Maximilians-Universität München, Am Coulombwall 1, 85748 Garching, Germany

²Max-Planck-Institut für Quantenoptik, Hans-Kopfermann-Strasse 1, 85748 Garching, Germany

*juergen.schmidt@physik.uni-muenchen.de

Abstract: High harmonic radiation is meanwhile nearly extensively used for the spectroscopic investigation of electron dynamics with ultimate time resolution. The majority of high harmonic beamlines provide linearly polarized radiation created in a gas target. However, circular polarization greatly extends the spectroscopic possibilities for high harmonics, especially in the analysis of samples with chirality or prominent spin polarization. We produced a free-standing multilayer foil as a transmission EUV quarter waveplate and applied it for the first time to high harmonic radiation. We measured a broadband (4.6 eV FWHM) ellipticity of 75% at 66 eV photon energy with a transmission efficiency of 5%. The helicity is switchable and the ellipticity can be adjusted to lower values by angle tuning. As a single element it can be easily integrated in any existing harmonic beamline without major changes.

©2015 Optical Society of America

OCIS codes: (260.5430) Polarization; (120.5410) Polarimetry; (230.4170) Multilayers; (340.7480) X-rays, soft x-rays, extreme ultraviolet (EUV).

References and links

1. S. H. Chew, F. Süßmann, C. Späth, A. Wirth, J. Schmidt, S. Zherebtsov, A. Guggenmos, A. Oelsner, N. Weber, J. Kapaldo, A. Gliserin, M. I. Stockman, M. F. Kling, and U. Kleineberg, "Time-of-flight-photoelectron emission microscopy on plasmonic structures using attosecond extreme ultraviolet pulses," *Appl. Phys. Lett.* **100**(5), 051904 (2012).
2. S. Neppel, R. Ernstorfer, A. L. Cavalieri, C. Lemell, G. Wachter, E. Magerl, E. M. Bothschafter, M. Jobst, M. Hofstetter, U. Kleineberg, J. V. Barth, D. Menzel, J. Burgdörfer, P. Feulner, F. Krausz, and R. Kienberger, "Direct observation of electron propagation and dielectric screening on the atomic length scale," *Nature* **517**(7534), 342–346 (2015).
3. R. L. Sandberg, A. Paul, D. A. Raymondson, S. Hädrich, D. M. Gaudiosi, J. Holtsnider, R. I. Tobey, O. Cohen, M. M. Murnane, H. C. Kapteyn, C. Song, J. Miao, Y. Liu, and F. Salmassi, "Lensless diffractive imaging using tabletop coherent high-harmonic soft-X-ray beams," *Phys. Rev. Lett.* **99**(9), 098103 (2007).
4. R. L. Sandberg, C. Song, P. W. Wachulak, D. A. Raymondson, A. Paul, B. Amirbekian, E. Lee, A. E. Sakdinawat, C. La-O-Vorakiat, M. C. Marconi, C. S. Menoni, M. M. Murnane, J. J. Rocca, H. C. Kapteyn, and J. Miao, "High numerical aperture tabletop soft x-ray diffraction microscopy with 70-nm resolution," *Proc. Natl. Acad. Sci. U.S.A.* **105**(1), 24–27 (2008).
5. A. L. Cavalieri, N. Müller, T. Uphues, V. S. Yakovlev, A. Baltuska, B. Horvath, B. Schmidt, L. Blümel, R. Holzwarth, S. Hendel, M. Drescher, U. Kleineberg, P. M. Echenique, R. Kienberger, F. Krausz, and U. Heinzmann, "Attosecond spectroscopy in condensed matter," *Nature* **449**(7165), 1029–1032 (2007).
6. E. Goulielmakis, Z.-H. Loh, A. Wirth, R. Santra, N. Rohringer, V. S. Yakovlev, S. Zherebtsov, T. Pfeifer, A. M. Azzeer, M. F. Kling, S. R. Leone, and F. Krausz, "Real-time observation of valence electron motion," *Nature* **466**(7307), 739–743 (2010).
7. F. Krausz and M. Ivanov, "Attosecond physics," *Rev. Mod. Phys.* **81**(1), 163–234 (2009).
8. E. Goulielmakis, V. S. Yakovlev, A. L. Cavalieri, M. Uiberacker, V. Pervak, A. Apolonski, R. Kienberger, U. Kleineberg, and F. Krausz, "Attosecond control and measurement: lightwave electronics," *Science* **317**(5839), 769–775 (2007).
9. R. Kienberger, E. Goulielmakis, M. Uiberacker, A. Baltuska, V. Yakovlev, F. Bammer, A. Scrinzi, T. Westerwalbesloh, U. Kleineberg, U. Heinzmann, M. Drescher, and F. Krausz, "Atomic transient recorder," *Nature* **427**(6977), 817–821 (2004).

10. P. B. Corkum, "Plasma perspective on strong field multiphoton ionization," *Phys. Rev. Lett.* **71**(13), 1994–1997 (1993).
11. K. C. Kulander, K. J. Schafer, and J. L. Krause, "Dynamics of short-pulse excitation, ionization and harmonic conversion," in *Super-Intense Laser-Atom Physics*, edited by B. Piraux, A. L'Huillier, and K. Rzaewski (Plenum, 1993)
12. K. S. Budil, P. Salières, A. L'Huillier, T. Ditmire, and M. D. Perry, "Influence of ellipticity on harmonic generation," *Phys. Rev. A* **48**(5), R3437–R3440 (1993).
13. P. Dietrich, N. H. Burnett, M. Ivanov, and P. B. Corkum, "High-harmonic generation and correlated two-electron multiphoton ionization with elliptically polarized light," *Phys. Rev. A* **51**, R3418 (1995).
14. N. H. Burnett, C. Kan, and P. B. Corkum, "Ellipticity and polarization effects in harmonic generation in ionizing neon," *Phys. Rev. A* **51**(5), R3418–R3421 (1995).
15. P. Antoine, A. L'Huillier, M. Lewenstein, P. Salières, and B. Carré, "Theory of high-order harmonic generation by an elliptically polarized laser field," *Phys. Rev. A* **53**(3), 1725–1745 (1996).
16. C. M. Schneider, M. S. Hammond, P. Schuster, A. Cebollada, R. Miranda, and J. Kirschner, "Observation of magnetic circular dichroism in uv photoemission from ferromagnetic fcc cobalt films," *Phys. Rev. B Condens. Matter* **44**(21), 12066–12069 (1991).
17. C. Boeglin, E. Beaulieu, V. Halté, V. López-Flores, C. Stamm, N. Pontius, H. A. Dürr, and J.-Y. Bigot, "Distinguishing the ultrafast dynamics of spin and orbital moments in solids," *Nature* **465**(7297), 458–461 (2010).
18. G. Schütz, M. Knütel, and H. Ebert, "Magnetic circular x-ray dichroism and its relation to local moments," *Phys. Scr. T* **49**, 302–306 (1993).
19. N. Böwering, T. Lischke, B. Schmidtke, N. Müller, T. Khalil, and U. Heinzmann, "Asymmetry in photoelectron emission from chiral molecules induced by circularly polarized light," *Phys. Rev. Lett.* **86**(7), 1187–1190 (2001).
20. Y. Liu, G. Bian, T. Miller, and T.-C. Chiang, "Visualizing electronic chirality and Berry phases in graphene systems using photoemission with circularly polarized light," *Phys. Rev. Lett.* **107**(16), 166803 (2011).
21. C.-H. Park and S. G. Louie, "Spin polarization of photoelectrons from topological insulators," *Phys. Rev. Lett.* **109**(9), 097601 (2012).
22. Y. Wang and N. Gedik, "Circular dichroism in angle-resolved photoemission spectroscopy of topological insulators," *Phys. Status Solidi Rapid Res. Lett.* **7**(1-2), 64–71 (2013).
23. J. Stöhr, Y. Wu, B. D. Hermsmeider, M. G. Samant, G. R. Harp, S. Koranda, D. Dunham, and B. P. Tonner, "Element-specific magnetic microscopy with circularly polarized x-rays," *Science* **259**, 658–661 (1993).
24. S. Eisebitt, J. Lüning, W. F. Schlotter, M. Lörger, O. Hellwig, W. Eberhardt, and J. Stöhr, "Lensless imaging of magnetic nanostructures by X-ray spectro-holography," *Nature* **432**(7019), 885–888 (2004).
25. O. Travnikova, J.-C. Liu, A. Lindblad, C. Nicolas, J. Söderström, V. Kimberg, F. Gel'mukhanov, and C. Miron, "Circularly polarized x rays: another probe of ultrafast molecular decay dynamics," *Phys. Rev. Lett.* **105**(23), 233001 (2010).
26. K. Holldack, J. Bahr, A. Balzer, U. Bovensiepen, M. Brzhezinskaya, A. Erko, A. Eschenlohr, R. Follath, A. Firsov, W. Frentrop, L. Le Guyader, T. Kachel, P. Kuske, R. Mitzner, R. Müller, N. Pontius, T. Quast, I. Radu, J.-S. Schmidt, C. Schübler-Langeheine, M. Sperling, C. Stamm, C. Trabant, and A. Föhlisch, "FemtoSpeX: a versatile optical pump-soft X-ray probe facility with 100 fs X-ray pulses of variable polarization," *J. Synchrotron Radiat.* **21**(5), 1090–1104 (2014).
27. G. L. Dakovski, P. Heimann, M. Holmes, O. Krupin, M. P. Minitti, A. Mitra, S. Moeller, M. Rowen, W. F. Schlotter, and J. J. Turner, "The soft x-ray research instrument at the linac coherent light source," *J. Synchrotron Radiat.* **22**(3), 498–502 (2015).
28. P. Antoine, B. Carré, A. L'Huillier, and M. Lewenstein, "Polarization of high-order harmonics," *Phys. Rev. A* **55**(2), 1314–1324 (1997).
29. X. Zhou, R. Lock, N. Wagner, W. Li, H. C. Kapteyn, and M. M. Murnane, "Elliptically polarized high-order harmonic emission from molecules in linearly polarized laser fields," *Phys. Rev. Lett.* **102**(7), 073902 (2009).
30. O. Kfir, P. Grychtol, E. Turgut, R. Knut, D. Zusin, D. Popmintchev, T. Popmintchev, H. Nembach, J. M. Shaw, A. Fleischer, H. Kapteyn, M. Murnane, and O. Cohen, "Generation of bright phase-matched circularly polarized extreme ultraviolet high harmonics," *Nat. Photonics* **9**(2), 99–105 (2014).
31. B. Vodungbo, A. Bartsch, J. Sardinha, J. Gautier, G. Lambert, C. Valentin, M. Lozano, G. Iaquaniello, F. Delmotte, S. Sebban, J. Lüning, and P. Zeitoun, "Polarization control of high order harmonics in the EUV photon energy range," *Opt. Express* **19**(5), 4346–4356 (2011).
32. J. B. Kortright and J. H. Underwood, "Multilayer optical elements for generation and analysis of circularly polarized x-rays," *Nucl. Instrum. Methods A* **291**(1-2), 272–277 (1990).
33. F. Schäfers, H.-Ch. Mertins, A. Gaupp, W. Gudat, M. Mertin, I. Packer, F. Schmolla, S. Di Fonzo, G. Soullié, W. Jark, R. Walker, X. Le Cann, R. Nyholm, and M. Eriksson, "Soft-x-ray polarimeter with multilayer optics: complete analysis of the polarization state of light," *Appl. Opt.* **38**(19), 4074–4088 (1999).
34. H. Kimura, T. Miyahara, Y. Goto, K. Mayama, M. Yanagihara, and M. Yamamoto, "Polarization measurement of SR from a helical undulator using a quarter wave plate for a wavelength of 12.8 nm," *Rev. Sci. Instrum.* **66**(2), 1920–1922 (1995).
35. C. La-O-Vorakiat, M. Siemens, M. M. Murnane, H. C. Kapteyn, S. Mathias, M. Aeschlimann, P. Grychtol, R. Adam, C. M. Schneider, J. M. Shaw, H. Nembach, and T. J. Silva, "Ultrafast demagnetization dynamics at the M edges of magnetic elements observed using a tabletop high-harmonic soft x-ray source," *Phys. Rev. Lett.* **103**(25), 257402 (2009).
36. J. B. Kortright and A. Fischer Colbrrie, "Standing wave enhanced scattering in multilayer structures," *J. Appl. Phys.* **61**(3), 1130 (1987).

37. B. L. Henke, E. M. Gullikson, and J. C. Davis, "X-ray interactions: photoabsorption, scattering, transmission and reflection at $E = 50\text{--}30000$ eV, $Z = 1\text{--}92$," *At. Data Nucl. Data Tables* **54**(2), 181–342 (1993).
38. A. L. Aquila, F. Salmassi, F. Dollar, Y. Liu, and E. Gullikson, "Developments in realistic design for aperiodic Mo/Si multilayer mirrors," *Opt. Express* **14**(21), 10073–10078 (2006).
39. M. Hofstetter, M. Schultze, M. Fieß, B. Dennhardt, A. Guggenmos, J. Gagnon, V. S. Yakovlev, E. Goulielmakis, R. Kienberger, E. M. Gullikson, F. Krausz, and U. Kleineberg, "Attosecond dispersion control by extreme ultraviolet multilayer mirrors," *Opt. Express* **19**(3), 1767–1776 (2011).
40. A. Guggenmos, S. Radünz, R. Rauhut, M. Hofstetter, S. Venkatesan, A. Wochnik, E. M. Gullikson, S. Fischer, B. Nickel, C. Scheu, and U. Kleineberg, "Ion polished Cr/Sc attosecond multilayer mirrors for high water window reflectivity," *Opt. Express* **22**(22), 26526–26536 (2014).
41. A. Guggenmos, R. Rauhut, M. Hofstetter, S. Hertrich, B. Nickel, J. Schmidt, E. M. Gullikson, M. Seibald, W. Schnick, and U. Kleineberg, "Aperiodic CrSc multilayer mirrors for attosecond water window pulses," *Opt. Express* **21**(19), 21728–21740 (2013).
42. K. Rabinovitch, L. R. Canfield, and R. P. Madden, "A method for measuring polarization in the vacuum ultraviolet," *Appl. Opt.* **4**(8), 1005–1010 (1965).
43. P. Dhez, "Polarizers and polarimeters in the X-UV range," *Nucl. Instrum. Methods* **261**(1-2), 66–71 (1987).
44. W. B. Westerveld, K. Becker, P. W. Zetner, J. J. Corr, and J. W. McConkey, "Production and measurement of circular polarization in the VUV," *Appl. Opt.* **24**(14), 2256–2262 (1985).
45. M. Fieß, M. Schultze, E. Goulielmakis, B. Dennhardt, J. Gagnon, M. Hofstetter, R. Kienberger, and F. Krausz, "Versatile apparatus for attosecond metrology and spectroscopy," *Rev. Sci. Instrum.* **81**(9), 093103 (2010).
46. E. Magerl, S. Neppel, A. L. Cavalieri, E. M. Bothschafter, M. Stanislowski, T. Uphues, M. Hofstetter, U. Kleineberg, J. V. Barth, D. Menzel, F. Krausz, R. Ernstorfer, R. Kienberger, and P. Feulner, "A flexible apparatus for attosecond photoelectron spectroscopy of solids and surfaces," *Rev. Sci. Instrum.* **82**(6), 063104 (2011).

1. Introduction

High harmonic generation (HHG) has become a versatile and indispensable tool for the spatio-temporal investigation of spin, charge and phonon dynamics with nanometer resolution in space [1–4] and unprecedented resolution in time down to attoseconds [5–9]. It enables the generation of broadband coherent radiation with a spectrum reaching to the extreme ultraviolet (EUV) or even up to the soft X-ray range from a table-top sized laser source. The commonly used and most established way so far to generate harmonic radiation is to focus a single near-infrared (NIR) pulsed laser beam with an intensity in the order of $10^{14}\text{--}10^{15}$ W/cm² into a noble gas target. A fraction of the gas atoms is tunnel ionized and the released electrons are subsequently accelerated in the laser field, gaining an energy amount which corresponds to multiples of the fundamental photon energy, before they collide and recombine with their parent ion, emitting a high energy photon [10,11]. This process is most efficient when the driving laser pulses are linearly polarized, giving the highest probability for recollision [12–14]. In this case, the polarization of the harmonic radiation is also linear [15]. Due to the high efficiency and the relatively easy constructional implementation of this concept, the majority of high harmonic sources are nowadays designed to provide linearly polarized harmonic radiation and circularly polarized high harmonic radiation is hardly available. However, high harmonic radiation with circular polarization greatly extends the (micro-) spectroscopic possibilities for this radiation and allows a more detailed and systematic investigation of specific classes of material systems, especially materials with chiral structure or pronounced electronic spin polarization, combined with the highest time resolution possible to date.

Currently, circularly polarized coherent EUV radiation is mainly provided by large scale synchrotron sources (e.g. helical undulators), and the applications of this radiation have already been extensively demonstrated, for instance, by EUV magnetic circular dichroism (XMCD) on magnetic [16–18] and nonmagnetic samples, photoelectron circular dichroism on chiral molecules [19,20] and spin resolved photoemission on topological insulators [21,22], magnetic coherent imaging and microscopy [23,24], by measuring quantum phases [20] and ultrafast decay dynamics [25]. However, the pulse duration of these sources and hence the time resolution in pump-probe experiments is still limited to ~ 100 femtoseconds [26]. This limit can be overcome by the current, fast progressing developments of free electron lasers, capable of providing brilliant soft X-ray radiation approaching the 10 fs range [27]. However, as a part of large scale facilities they cannot be considered as a widespread alternative for the table-top sized HHG sources.

Due to this eminent usefulness of circularly polarized EUV/soft X-ray radiation and the outstanding advantages of high harmonic radiation regarding high time resolution and large spectral bandwidth, there is a strong motivation to generate harmonic radiation with circular polarization, or at least with elliptical polarization and a high degree of ellipticity. Several concepts have been developed to meet this demand including both direct techniques which aim to produce harmonics with circular polarization directly from the HHG process and X-ray optical techniques transforming linear polarization into circular polarization. The earliest approach suggests the usage of elliptically polarized laser pulses to drive the harmonic generation process. Here, the highest harmonic ellipticity could be achieved for low energy harmonics in the plateau region below 40 eV from neon [28]. However, as the recombination probability for the ionized electrons quickly drops to zero with increasing degree of elliptical polarization of the driving laser pulse [12], this approach is highly inefficient, especially for high energy harmonics. Another method employs non-isotropic gas media such as aligned molecules to break the cylindrical symmetry around the laser polarization axis. This gives rise to elliptically polarized high harmonic emission even from linearly polarized driver pulses. Experimentally, only a moderate harmonic ellipticity up to 0.4 could be measured from aligned N₂ molecules [29]. Efficient generation of circularly polarized high harmonics was recently demonstrated using co-propagating bichromatic driver pulses, both with circular polarization but of opposite handedness [30]. Harmonic radiation with high ellipticity could also be achieved using reflective waveplates, consisting of multiple metal mirrors, with an overall efficiency of few percent [31]. However, both concepts require additional constructional effort in their implementation and substantially more alignment work. Bichromatic driver pulses generally have to be guided on separate beam paths for their independent adjustment of dedicated beam parameters and have to be accurately overlapped in space and time at the gas target. Multi-element reflective waveplates are spacious and challenging to align as well.

Here we present the generation of circularly polarized high harmonic radiation using transmission multilayer waveplates. Although transmission waveplates are conventional in the visible and NIR spectral range they are quite extraordinary in the EUV and soft X-ray range due to the lack of strongly birefringent materials and the generally high absorption rate of any material in that energy range. Nevertheless, the usage and applicability of multilayer structures in transmission as phase retarders in order to generate and analyze circularly polarized X-rays was already proposed more than two decades ago [32] and tested with synchrotron radiation [33,34]. However, to our knowledge they have never been applied to any high harmonic source so far. We have designed, produced and characterized a substrateless multilayer quarter waveplate for high harmonic radiation at 66 eV photon energy for an exemplary XMCD application at the nickel (Ni) M-edge [35]. We measured a broadband ellipticity of 75% at a transmission efficiency of nearly 5%. By selecting the proper material systems and engineering the parameters of the multilayer structure, the waveplate can be designed for various energy ranges. Suitable material combinations for transmission phase retarders have been shown for energies up to the water window [33]. Furthermore, by simple angle tuning of the waveplate, its working energy range can be shifted by several eV around the design energy. This can be very useful to either adapt its functionality to nearby photon energies, e.g. to an adjacent harmonic peak, or to adjust the degree of ellipticity at a certain photon energy. Besides, the helicity is easily switchable by changing the azimuthal alignment angle by 90°. The major advantage of our waveplate, however, lies in the fact that it is a small single-element device of only 1 inch size, allowing it to be easily incorporated in any existing standard HHG beamline without any major constructional changes, upgrading it to circularly polarized radiation without deviating the original beam direction.

2. Waveplate design and fabrication

A phase shift of 90° between two perpendicular decomposed field components of the same amplitude has to be introduced in order to transform linear polarization into circular. It has been found that a multilayer structure being used in transmission can introduce a substantial

phase shift between s- and p-orientated field components near its Bragg angle if this angle is in the vicinity of the Brewster angle, which is close to 45° in the case of EUV [32]. In this case standing waves are formed due to interference of the incoming and reflected s-polarized field within the periodic multilayer structure whose intensity is either concentrated in the spacer material for angles slightly smaller than the Bragg angle or in the absorber material for angles slightly larger than the Bragg angle [36]. This gives rise to a strong phase retardation or phase advance, respectively, for the s-component, basically through refractive effects, whereas the p-component remains unaffected by this resonance due to its proximity to the Brewster angle. Based on this behavior we designed a Mo/Si (molybdenum/silicon) multilayer structure which creates the desired phase shift at an incident angle of 45° and at a photon energy of 66 eV while simultaneously transmitting the s- and p-component at equal amplitude values. The composition of the multilayer stack design is depicted in Fig. 1.

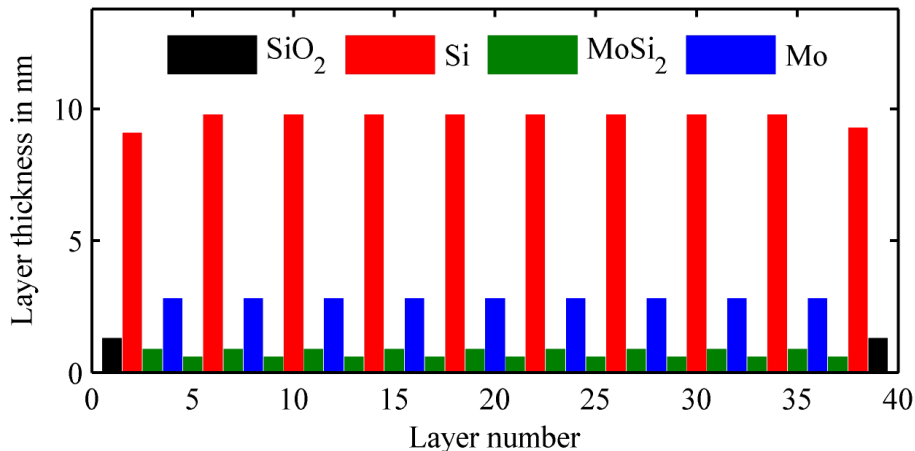


Fig. 1. Composition of the multilayer stack. The real stack design starts and ends with a natively formed SiO₂ layer. Asymmetric MoSi₂ layers are formed by material reaction at the Mo-Si-Mo interfaces. Their thickness depends on whether Mo is deposited on Si or vice versa [38]. The fraction of the absorber material Mo is kept small in comparison to the spacer material Si to minimize the waveplate's absorption.

The design energy of 66 eV was chosen to demonstrate a test case for a realistic XMCD application at the Ni M-edge (binding energies of 66.2 eV and 68 eV). The calculated spectral behavior of the given multilayer stack is shown in Fig. 2. Optical constants for the simulation are taken from [37]. Oxide layers, roughness values as well as interdiffusion and interface reaction parameters are included in the simulation model and are based on long-term experience in the production of EUV/soft X-ray multilayer optics [39–41].

As can be seen from the simulation, the s- and p-transmission curves intersect at the design energy with an absolute value of almost 5%. The corresponding phase shift is close to 90° . The drop-off in s-transmission at 70 eV constitutes the Bragg reflection peak for the given angle of incidence.

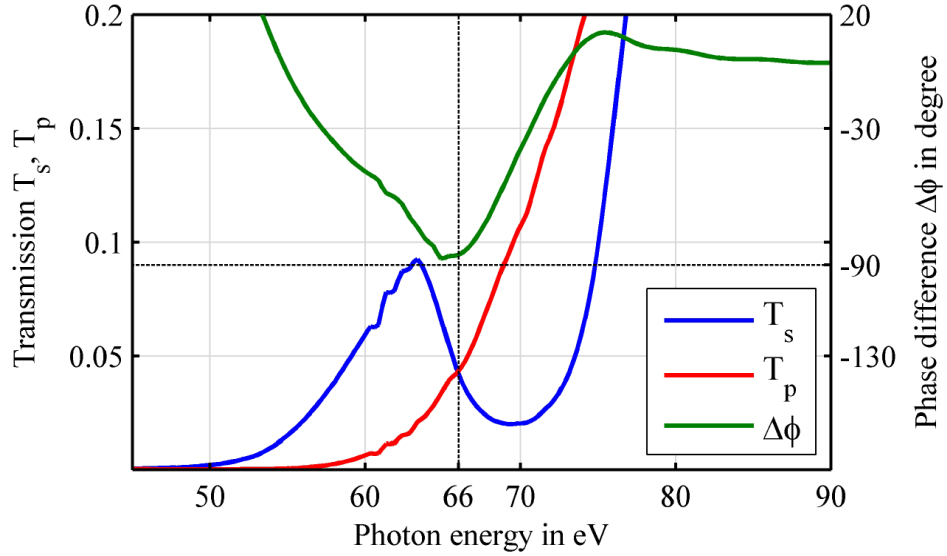


Fig. 2. Simulated spectral transmission behavior and phase difference between s- and p-polarization of the EUV multilayer waveplate for an angle of incidence of 45° . For this angle the Bragg condition for the given multilayer stack is fulfilled at an energy of approximately 70 eV, which results in a local transmission minimum at that energy. The waveplate is designed for a nominal photon energy of 66 eV where T_s equals T_p and a phase shift of nearly 90° is introduced.

From the transmission and phase behavior the respective spectral ellipticity ε and orientation Φ of the polarization ellipse are deduced and plotted in Fig. 3 for different incident angles. The ellipticity at 66 eV reaches almost the ideal value of 1 (circular polarization) while it starts dropping for nearby energies. However, the spectral full width at half maximum (FWHM) bandwidth of the ellipticity curve is with 4 eV remarkably high, indicating that pulse durations in the (sub-) femtosecond regime are still supported with a high degree of ellipticity. The steep slope in the orientation angle around 66 eV reveals a strong sensitivity with respect to photon energy and incident angle.

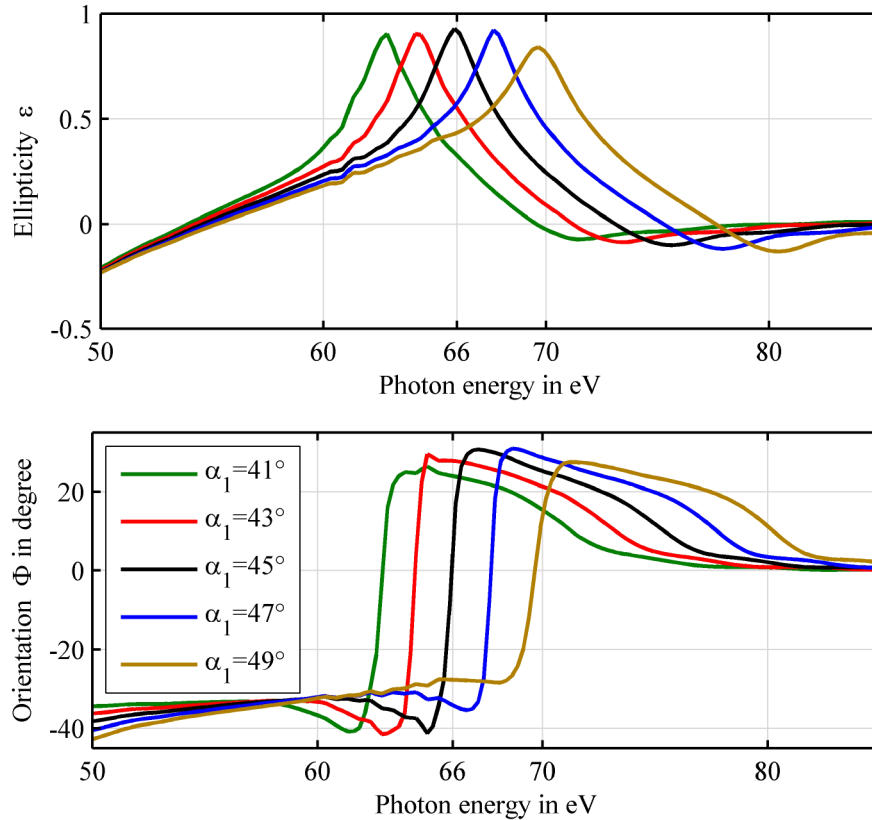


Fig. 3. Calculated spectral ellipticity and polarization orientation of the transmitted radiation for different normal incident angles α_1 . The polarization before the waveplate is linear horizontal. The ellipticity at 66 eV and $\alpha_1 = 45^\circ$ is nearly 1. The peak ellipticity can be shifted by several eV in energy while its magnitude is only little affected by varying the incident angle.

An important and critical issue in the development of transmission multilayer structures is the fabrication procedure. In contrast to earlier approaches, our waveplate was not fabricated on a supporting foil (e.g. silicon nitride) but was designed as a free-standing multilayer foil for best transmission efficiency. It has a total thickness below 150 nm and spans a free aperture as large as 3 mm. The foil is attached to a 1 inch metal ring to fit in any standard optical mount.

While the production of high quality reflection multilayer structures, which are placed on a super-polished solid substrate, is well developed, high quality free-standing transmission multilayer optics are challenging to fabricate and require special attention regarding stability and film stress compensation. The fabrication process was optimized to produce transmission multilayers with a reasonably good quality and is depicted in Fig. 4. All fabrication steps were done in a class 1000 clean room environment in order to keep the contamination level during sample handling as low as possible. As temporary substrate we used a semiconductor grade silicon wafer which is spin-coated with a PMMA (polymethyl methacrylate) resist (thickness: 290 nm) and baked at 130°C. The multilayer structure was applied on top of the resist by ion beam deposition where each layer thickness can be controlled with sub-nm precision [41].

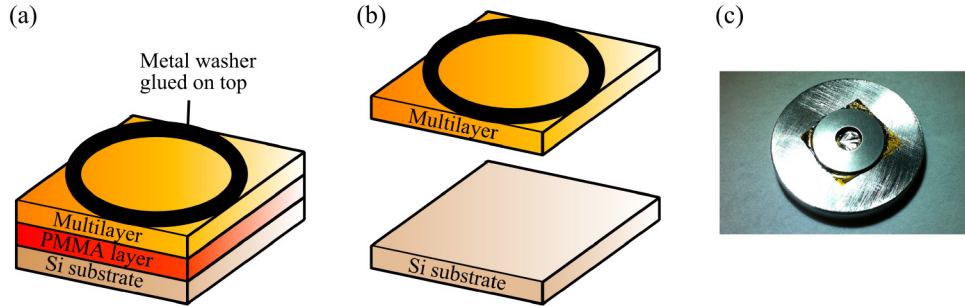


Fig. 4. Fabrication process of the free-standing EUV quarter waveplate. (a): Raw sample with multilayer coating deposited on a PMMA coated Si substrate. (b): By dissolving the PMMA resist, the multilayer stack is carefully removed from the auxiliary Si substrate. (c): Image of the actual device.

The sputter times have been modified to account for interface reactions, interdiffusion and roughness effects as well as post-deposition oxide formation (see Fig. 1). In the next step the metal ring was glued onto the structure. For an improved stability, a thin adhesive Kapton foil was placed between the multilayer stack and the metal ring to reduce stress on the multilayer structure introduced by the glue during its curing time. Finally, the resist was dissolved by an appropriate solvent and the silicon wafer was carefully removed. In order to remove any remaining debris from the solvent, the entire assembly was baked out at 100°C for one hour in the last step. It has to be mentioned that due to interface and surface stress, the multilayer foil is usually not perfectly even, but slightly wavy.

3. Measurements and results

In order to verify the proper functioning of the waveplate, we first measured its spectral transmission in s- and p-orientation at our HHG beamline. Few-cycle driver pulses, centered at 780 nm, generate high harmonic radiation in a neon gas jet with horizontal, linear polarization. Aluminum (Al) filters with thicknesses in the 200–400 nm range, were utilized to block the fundamental laser beam. The spectrum was measured by a EUV spectrometer using a concave, aberration corrected flat-field grating with a EUV CCD camera as a detector. For this measurement the laser intensity was adjusted so that the spectral measurement range was close to the continuous cut-off region of the harmonic spectrum where the modulation depth for distinct harmonic peaks is greatly reduced. The transmitted spectra are finally divided by a reference spectrum which was taken without the waveplate in order to obtain the pure spectral transmission characteristics of the waveplate. The nominal angle of incidence was 45° with an error of $\pm 0.5^\circ$. Figure 5 shows the result in an energy range around the design energy. The measurement fits well to the simulation as characteristic features are well reproduced. In s-orientation the local peak near to 63 eV and the minimum at 70 eV, constituting the Bragg reflection condition, is clearly replicated while in p-orientation the transmittance is monotonically increasing over the depicted energy range, in coincidence with the simulation.

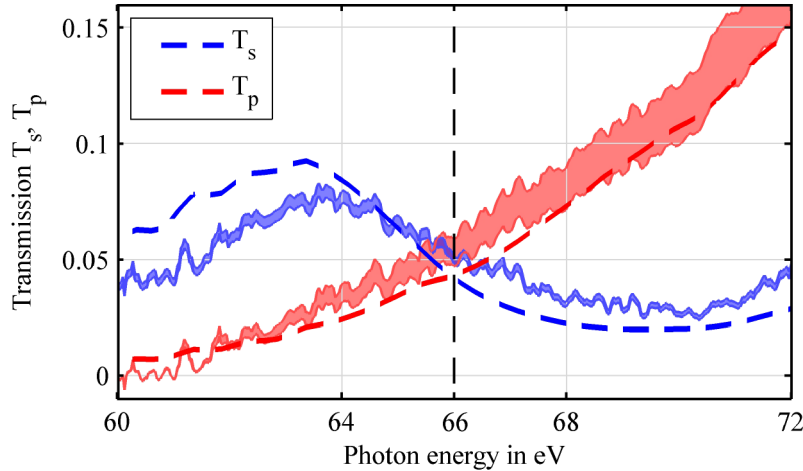


Fig. 5. Measured transmission of the waveplate in s (blue)- and p (red)-orientation together with the respective simulations (dashed curves). The shaded area represents the error interval which is caused by a drift in the harmonic intensity during the acquisition time.

The slight shift in energy of the local peak transmittance in s-orientation is attributed to a small alignment error in the angle of incidence. The shaded area represents the error interval induced by a slight drift of the harmonic intensity over time. The mean transmission efficiency within the measurement error is approximately 5%.

Next, we determined the polarization state, i.e. ellipticity and orientation, of the harmonic radiation after inserting the waveplate into the beam path. Ellipticity and polarization orientation are a direct consequence of the introduced phase shift. Therefore we performed a simplified polarimetry measurement by recording the beam intensity after a rotating polarizer as a function of its polarization axis β_2 (Rabinovitch setup [42]) while keeping the azimuthal angle β_1 of the waveplate at a fixed value. For this, a multilayer mirror has been designed as a polarization analyzing element which only reflects radiation in s-orientation but not in p-orientation. The geometry of the measurement setup is shown in Fig. 6.

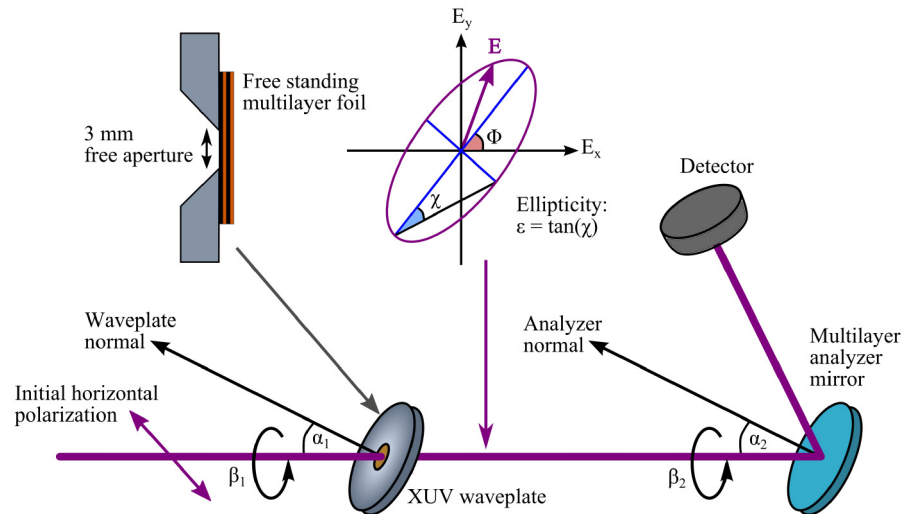


Fig. 6. Geometrical setup of the polarimetry measurement. Waveplate and analyzer mirror can be rotated around the beam axis by β_1 and β_2 as well as tilted by α_1 and α_2 , respectively. The initial EUV polarization before the waveplate is linear horizontal, after transmission through the waveplate the E-field vector describes an ellipse with ellipticity ε and orientation Φ .

In the following we introduce a reference (x,y)-coordinate system which is set by the direction of initial laser polarization, which is nearly horizontal, coinciding with the x-axis. Azimuthal angles along the beam axis are positive for counter-clockwise rotation when viewed in beam direction. A second (s,p)-coordinate system is firmly attached to each optical element with s-axis being perpendicular and p-axis parallel to the plane of incidence.

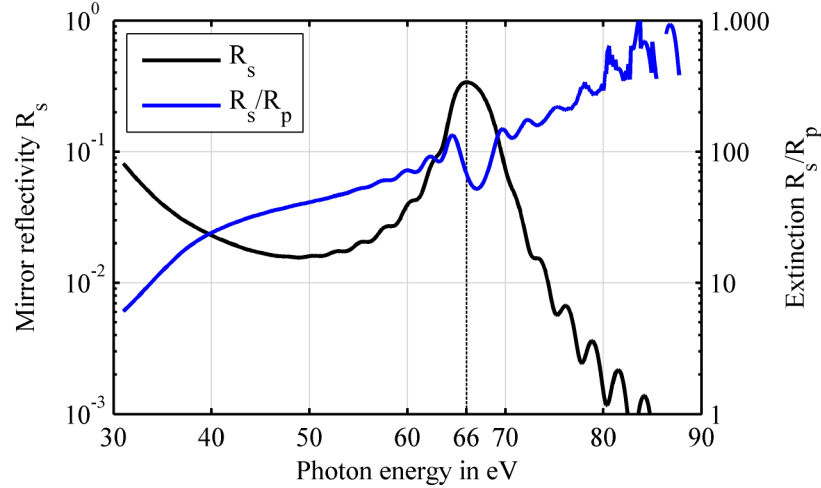


Fig. 7. Calculated spectral behavior of the analyzer multilayer mirror. The peak reflectivity in s-orientation is 34% at 66 eV with a FWHM reflection bandwidth of 4.6 eV. The extinction ratio within this bandwidth is larger than 50.

The analyzer multilayer mirror has been designed for the same nominal energy as the waveplate. The simulated spectral behavior of the mirror is plotted in Fig. 7. The reflectivity for s-polarization has a peak value of 34% at 66 eV and a reflection bandwidth of 4.6 eV (FWHM) supporting sub-fs pulses. The analyzer mirror was operated near the Brewster angle in order to suppress reflections in p-orientation [43]. Also shown is the extinction ratio R_s/R_p , i.e. the suppression factor of p-reflectivity compared to s-reflectivity, which is larger than 50 within the reflection bandwidth. Both optical elements, the waveplate and the analyzer mirror, were mounted on motorized gimbal mounts enabling the independent adjustment of both their incident angles $\alpha_{1,2}$ and their azimuthal angles $\beta_{1,2}$ around the beam axis. The complete polarization state of light is commonly described by the four Stokes parameters, real quantities with the dimension of intensity, which are combined to the Stokes vector $\mathbf{s} = (s_0, s_1, s_2, s_3)^T$ (vectors in inline equations are denoted in bold letters), where s_0 describes the total intensity, s_1 the fraction of linear horizontal and vertical polarization, s_2 the fraction of linear polarization rotated by $\pm 45^\circ$ and s_3 the fraction of circular left- and right-handed polarization. The polarization degree P is given by

$$P = \frac{\sqrt{s_1^2 + s_2^2 + s_3^2}}{s_0} = \frac{s_0 - s_{np}}{s_0}, \quad (1)$$

where $s_{np} = s_0 - \sqrt{s_1^2 + s_2^2 + s_3^2}$ is the unpolarized fraction. The ellipticity ε and orientation Φ of the polarization ellipse are then obtained by [28]

$$\varepsilon = \text{sgn}(s_3) \sqrt{\frac{s_0 - s_{np} - \sqrt{s_1^2 + s_2^2}}{s_0 - s_{np} + \sqrt{s_1^2 + s_2^2}}}, \quad (2)$$

$$\tan(2\Phi) = \frac{s_2}{s_1}. \quad (3)$$

Any interaction with an optical element is described in this formalism by the Mueller matrix [44]

$$M = \frac{1}{2}(R_p + R_s) \begin{pmatrix} 1 & -\cos(2\Psi) & 0 & 0 \\ -\cos(2\Psi) & 1 & 0 & 0 \\ 0 & 0 & \sin(2\Psi)\cos\Delta & \sin(2\Psi)\sin\Delta \\ 0 & 0 & -\sin(2\Psi)\sin\Delta & \sin(2\Psi)\cos\Delta \end{pmatrix}, \quad (4)$$

where $\tan\Psi = r_p/r_s$ for reflecting and $\tan\Psi = t_p/t_s$ for transmitting optics and Δ is the induced phase shift between s- and p-orientation. The Mueller matrix which rotates the coordinate system by an angle β around the beam axis is

$$R(\beta) = \begin{pmatrix} 1 & 0 & 0 & 0 \\ 0 & \cos\beta & \sin\beta & 0 \\ 0 & -\sin\beta & \cos\beta & 0 \\ 0 & 0 & 0 & 1 \end{pmatrix}. \quad (5)$$

Let the polarization state after the waveplate be \mathbf{s}_i , then the Stokes vector \mathbf{s}_f after reflection from the analyzer mirror at angle β_2 is obtained by

$$\vec{s}_f = R(-\beta_2) \cdot M \cdot R(\beta_2) \cdot \vec{s}_i. \quad (6)$$

The back rotation of the coordinate system by the third Mueller matrix is necessary in order to obtain the polarization state in the original reference frame, defined by the incident laser coordinate system. The intensity which is recorded by the detector during a β_2 -scan is given by the first component of \mathbf{s}_f :

$$s_{f0} = (R_p + R_s) \left(\frac{1}{2}s_0 - \frac{1}{2}s_1 \cos(2\Psi)\cos(2\beta_2) - \frac{1}{2}s_2 \cos(2\Psi)\sin(2\beta_2) \right), \quad (7)$$

which can be rewritten using Eq. (3) and the definition for $\tan\Psi$ as

$$I(\beta_2) = \frac{1}{2}(R_p + R_s)s_0 - \frac{1}{2}(R_s - R_p)\sqrt{s_1^2 + s_2^2} \cos(2\beta_2 + 2\Phi). \quad (8)$$

The result is a sinusoidal curve whose modulation depth encodes the ellipticity and whose phase shift represents the orientation. This means in detail that any linearly polarized light field results after a β_2 -scan in a curve with the highest modulation strength which in turn is determined by the characteristics of the analyzer as it ranges from the maximum value of $R_s s_0$ to the minimum value of $R_p s_0$, while the polarization direction is given by the phase shift according to Φ in the cosine term. A fully circularly polarized light field on the other hand does not give any modulation at all, i.e. a β_2 -scan yields a constant value of $I = 0.5(R_p + R_s)s_0$. Also note that the Stokes component s_3 is not directly accessible in this simplified polarimetry measurement since the azimuthal angle β_1 of the waveplate is not varied. Therefore, the amount of unpolarized light is not determined and only an upper bound for the ellipticity can be obtained, as discussed in [28], by

$$\mathcal{E}_{max} = \sqrt{\frac{s_0 - \sqrt{s_1^2 + s_2^2}}{s_0 + \sqrt{s_1^2 + s_2^2}}} \quad (9)$$

which equals the true ellipticity from Eq. (2) for fully polarized light, i.e. for $P = 1$. However, as can easily be verified from Eq. (9) and (2), the deviation of ε_{\max} from ε becomes negligibly small for large values of s_3 , i.e. a high degree of circular polarization. It only starts becoming significant for small s_3 values, provided the ratio between s_{np} and s_0 is constant. The latter requirement is true in our case as the conditions of the harmonic generation process are not altered throughout the measurements. Using the maximum and minimum value of Eq. (8), namely

$$I_{\min/\max} = \frac{1}{2}(R_p + R_s)s_0 \pm \frac{1}{2}(R_s - R_p)\sqrt{s_1^2 + s_2^2}, \quad (10)$$

Equation (9) is recast to

$$\varepsilon_{\max} = \sqrt{\frac{R_s I_{\min} - R_p I_{\max}}{R_s I_{\max} - R_p I_{\min}}} \quad (11)$$

and the ellipticity is directly obtained from the intensity modulation depth of the β_2 -scan. The ratio R_s/R_p is obtained by the same scan but without the waveplate. The value $\beta_2 = 0^\circ$ corresponds to s-orientation of the analyzer mirror regarding the initial linear polarization direction. A critical issue for this measurement is the proper pre-filtering of the harmonic radiation as will be shown in more detail in the following section.

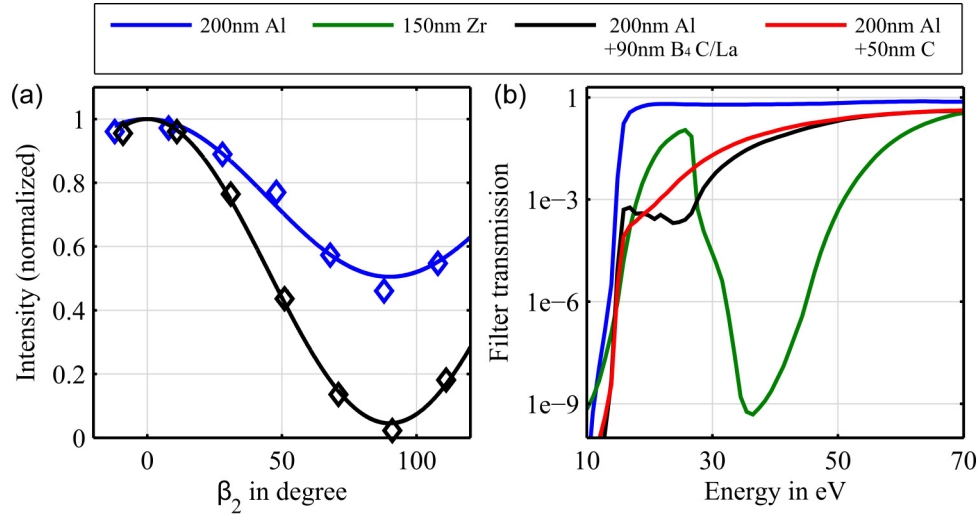


Fig. 8. (a): β_2 -scan without the waveplate using different metal filters to block the IR beam and to pre-filter the harmonic radiation. For the standard Al filter, the effective extinction of the analyzer mirror is reduced to about 2 since the fraction of transmitted radiation from the low energy range < 40 eV, where the mirror loses its polarizing capability (Fig. 7), is still too high. Material combinations of Al/B₄C/La or Al/C show a better suppression of radiation in that energy range, leading to an improved effective extinction close to the value expected from the simulated design of the mirror at 66 eV. (b): Spectral transmission behavior of different filter materials. The standard Al and Zr filters exhibit a strong transmission window at low photon energies ≤ 40 eV. Higher suppression in this range is achieved by adding the materials La and/or C.

First we have tested the polarization capability of the analyzing multilayer mirror. As is usual for high harmonic measurements, we used a thin metal foil to block the NIR driver pulse and separate it from the high harmonic EUV radiation [45,46]. As can be seen from the calculation in Fig. 7 the analyzer mirror loses its polarizing capability, i.e. the extinction ratio decreases significantly for low energy harmonics below 40 eV while at the same time its reflectivity increases for that energy range. This behavior is destructive for the measurement

and it has to be ensured that radiation in this energy range is sufficiently suppressed. Unfortunately, standard Al and Zr (Zirconium) filters which are routinely used to block the NIR driver are not appropriate, as obvious from the two β_2 -scans shown in Fig. 8(a). Both scans were done without the waveplate but with different filter combinations. As the polarization of the radiation hitting the mirror is linear in this case, the ratio between the maximum value at $\beta_2 = 0^\circ$, corresponding to s-orientation, and the minimum at $\beta_2 = 90^\circ$, corresponding to p-orientation, directly represents the extinction of the analyzer mirror, provided that the polarization degree equals 1. In the case of the Al filter the extinction is only about 2 and hence far off from the simulated expectation value plotted in Fig. 7. A similar result is obtained with Zr filters. This is because both filter options still show a strong transmission window between 20 eV and 40 eV where reflectivity in p-orientation is not sufficiently suppressed by the mirror. Effectively, leakage of radiation in this low energy range has the same effect on the measurement as unpolarized radiation, centered around the nominal energy of 66 eV, would have. In order to investigate which case is true we have tested filter combinations of Al/La (lanthanum)/B₄C (boron carbide) and Al/C (carbon) which better suppress the low energy part. As can be seen from the β_2 -scans in Figs. 8(a) and 9(a) the effective extinction of the analyzer mirror substantially improves and is close to the calculated value.

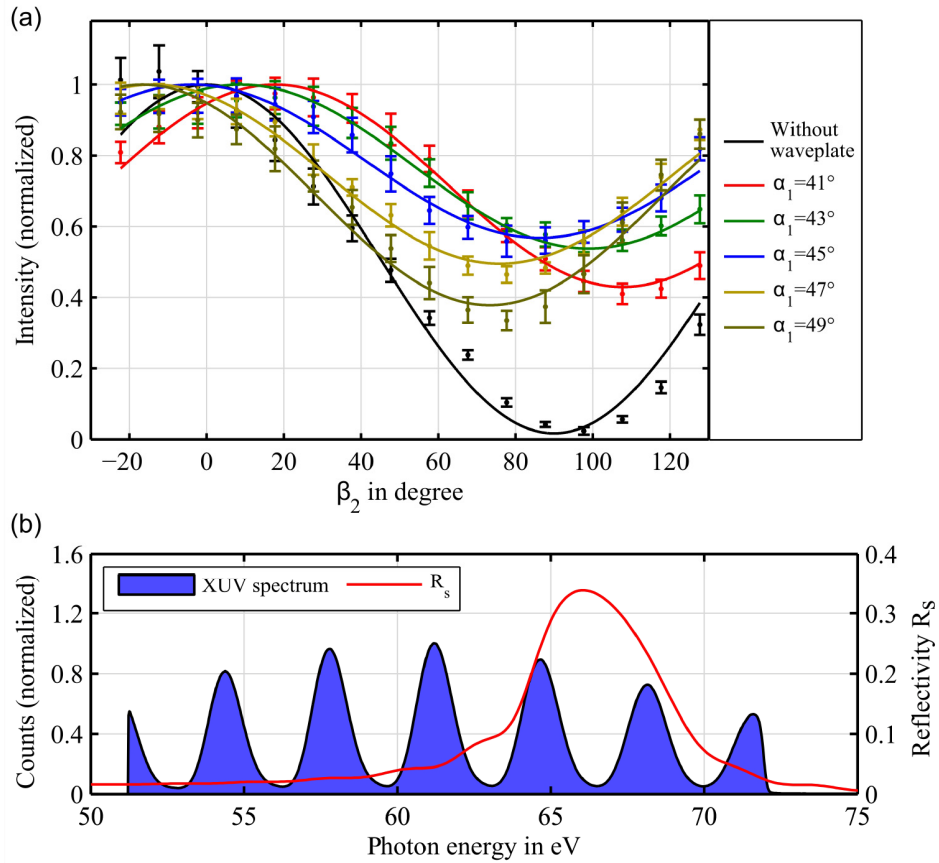


Fig. 9. (a): Results for the β_2 -scans without and with the waveplate for different detuning angles. The larger the detuning angle, the stronger the modulation depth (the smaller the ellipticity) and the stronger the shift in β_2 . An Al/C filter was used to pre-filter the high harmonic radiation (b): Measured EUV harmonic spectrum as used for the β_2 -scans and for the simulation values for the ellipticity $\epsilon_{\text{simulated}}$ and orientation angle $\Phi_{\text{simulated}}$. Two neighboring harmonic peaks are cut out by the bandwidth of the analyzer mirror.

Although the filter combination with La shows a better suppression than the Al/C filter, see Fig. 8(b), we have chosen the latter throughout the measurement since La is subject to fast oxidation. Therefore, all of the following measurements were performed with a 200 nm Al and 50 nm C filter combination which is chemically more stable and easier to implement.

For the polarimetry measurement we first experimentally determined the effective extinction of the analyzer by a β_2 -scan without waveplate, then we measured β_2 -scans with inserted waveplate at a fixed azimuthal angle $\beta_1 = -45^\circ$ and a nominal incident angle $\alpha_1 = 45^\circ$ as well as at an angle detuning of $\pm 2^\circ$ and $\pm 4^\circ$. The absolute angle uncertainty of the waveplate is $\pm 0.5^\circ$. The results are plotted in Fig. 9(a). For each scan we fit a curve according to Eq. (8) and normalize it for a better visualization. The extinction of the analyzer is determined to be 60, in good agreement with the simulation, hence the fraction of unpolarized radiation or, equivalent, low energy radiation that leaks through the filter can be assumed to be small. The depicted error is three times the standard deviation of 5000 laser shots. Using Eq. (11) and the measured extinction value, we can easily deduce the ellipticity from the fitted curves. The orientation of the polarization ellipse is obtained by the β_2 -offset of the I_{\max} value for each curve compared to the curve measured without the waveplate. The results are summarized in Table 1.

The simulated values are obtained by calculating the intensity curve $I_{\text{sim}}(\beta_2)$ of a β_2 -scan using the actual spectral harmonic intensity distribution, depicted in Fig. 9(b), and the simulated transmission and reflection behavior of the waveplate and the mirror, at the given azimuthal and incident angles. From the obtained theoretical $I_{\text{sim}}(\beta_2)$ curves, we extract the ellipticity and orientation in the same manner as from the measured curves.

Table 1. Summary of measured and simulated values for the ellipticity ϵ and orientation Φ of the EUV radiation after transmission through the waveplate at different incident angles α_1 .

| α_1 | $\epsilon_{\text{measured}}$ | $\epsilon_{\text{simulated}}$ | Φ_{measured} | $\Phi_{\text{simulated}}$ |
|------------|------------------------------|-------------------------------|--------------------------|---------------------------|
| 41 | 0.64 | 0.43 | + 18 | + 19 |
| 43 | 0.73 | 0.60 | + 9 | + 18 |
| 45 | 0.75 | 0.79 | -4 | -2 |
| 47 | 0.69 | 0.68 | -14 | -26 |
| 49 | 0.60 | 0.54 | -17 | -28 |

It has to be mentioned that this simulation does not include any unpolarized radiation. As expected, for increasing angle detuning the ellipticity decreases and the orientation angle starts strongly deviating from the original linear polarization direction.

4. Discussion and conclusion

The measured results for the ellipticity and orientation angle clearly show the tendency as expected from the theoretical design. For the nominal angle of incidence of 45° the measured ellipticity well reproduces the simulated value within an error of 5%. This proves the proper behavior of our free-standing multilayer foil as a transmissive EUV quarter waveplate. Detuning the incident angles decreases the degree in ellipticity for the fixed photon energy of 66 eV (central energy of the analyzer mirror) and hence detunes the spectral bandwidth of polarization (as simulated in Fig. 3). The fact that for the detuned incident angles the deviation between measured and simulated ellipticity values increases encourages the assumption that there is a small fraction of either unpolarized light, or more likely, leakage of low energy radiation through the filter which is still strong enough to affect the measurement. Both have the same impact on our measurement and can be simply denoted as effectively unpolarized fraction of the radiation. This fraction can be assumed to be constant throughout the measurement independent on the angle tuning of the waveplate. Only the relative magnitudes between s_1 , s_2 and s_3 are affected by angle tuning. When plotting the ratio ϵ/ϵ_{\max} as a function of s_3 while leaving s_{np} constant, it becomes obvious that ϵ_{\max} approaches ϵ for high values of s_3 , i.e. for a high fraction of circular polarization. Therefore, we can assume that the obtained value $\epsilon_{\max} = 0.75$ for $\alpha_1 = 45^\circ$ is close to the true value ϵ .

We showed that the orientation angles switch sign for different detuning directions as expected. Any offset between measured and simulated values is attributed to the adjustment uncertainty of α_1 . As mentioned above, the orientation angle is quite sensitive to α_1 due to its steep slope around the design energy as shown in Fig. 3. Another source of error regarding angle alignment is the slightly wavy surface of the multilayer foil which was not taken into account in the simulation, but could possibly give an additional effective angle alignment error.

Another aspect which is of high interest is the effect of the waveplate on the temporal structure of the EUV input pulses. The broad reflectivity bandwidth of our analyzer supports fourier-transform limited pulses with a duration of 400 as. However, nonlinear spectral phase distortions induced by the waveplate lead to pulse broadening, temporal reshaping and chirping. We also have investigated from our simulations the second order phase effect, i.e. group delay dispersion (GDD), the predominant phase effect for temporal pulse broadening, on the input pulses while passing through the waveplate. We obtained a GDD value of 33000 as² when the light field is p-orientated which would broaden the pulse to about 460 as. This amount of broadening is comparable to the one caused by a single slab of thin metal foil with a thickness similar to our waveplate. However, the situation is quite different for the s-orientation of the light field. As in this case standing waves are formed within the multilayer structure, which induce the required phase delay toward the p-component, a much higher GDD value of -1.24 fs² is obtained for this orientation which broadens the pulse to about 8.5 fs.

In this work we have demonstrated for the first time the successful implementation of a substrate-less multilayer transmission quarter waveplate for HHG. To achieve the highest transmission efficiency it was fabricated as a free-standing foil without any support. A high broadband ellipticity of 0.75 was measured in accordance with the theoretical design. The used bandwidth of 4.6 eV FWHM supports pulses in the low femtosecond regime, necessary for an ultrafast time resolution. For narrow bandwidth applications which are tuned to a single harmonic peak or even to a fraction of that, higher ellipticities up to 1 can be expected. Although we could not measure the sign of helicity with our setup, it is obvious that the handedness of circular polarization can be easily switched by adjusting the azimuthal angle β_1 to either $+45^\circ$ or -45° with respect to the initial polarization direction. Our waveplate is a space-saving, single element which can easily be integrated in any existing standard HHG beamline with linear polarization, upgrading it for circular polarization with all its benefits, without the need for altering the conditions of the harmonic generation process. Complex additional arrangements are not necessary with this approach.

Acknowledgment

We thankfully acknowledge scientific support and valuable discussions by Ferenc Krausz (MPQ, LMU). This work was financially supported by the Deutsche Forschungsgemeinschaft (DFG) by the Excellence Cluster Munich-Centre for Advanced Photonics (MAP, EXC 158).